Communications in Nonlinear Science and Numerical Simulation 114 (2022) 106696

Contents lists available at ScienceDirect

Communications in Nonlinear Science and Numerical Simulation

journal homepage: www.elsevier.com/locate/cnsns

Research paper

Optimising the locomotion of a vibro-impact capsule robot self-propelling in the small intestine

Yao Yan [a], Baoquan Zhang [a], Joseph Páez Chávez [b,c], Yang Liu [d,*]

[a] School of Aeronautics and Astronautics, University of Electronic Science and Technology of China, 611731, China
[b] Center for Applied Dynamical Systems and Computational Methods (CADSCOM), Faculty of Natural Sciences and Mathematics, Escuela Superior Politécnica del Litoral, P.O. Box 09-01-5863, Guayaquil, Ecuador
[c] Center for Dynamics, Department of Mathematics, TU Dresden, D-01062 Dresden, Germany
[d] College of Engineering, Mathematics and Physical Sciences, University of Exeter, Exeter, EX4 4QF, UK

ARTICLE INFO

Article history:
Received 16 March 2022
Received in revised form 28 June 2022
Accepted 30 June 2022
Available online 4 July 2022

Keywords:
Vibro-impact
Piecewise-smooth dynamical system
Self-propulsion
Capsule robot
Intestinal resistance

ABSTRACT

Circular fold is one of the biggest barriers for resisting endoscopic robots moving in the small intestine. Overcoming such a resistance force for progression during endoscopic procedure may significantly improve diagnostic efficiency. This paper studies the locomotion of a vibro-impact capsule robot self-propelled on a small intestine substrate when encounters various types of circular folds. A new capsule-fold model is developed to understand capsule-fold interaction and determine the optimum control parameters (the frequency and amplitude of excitation) for a successful crossing motion. Extensive bifurcation analyses show that the geometry and mechanical properties of the circular folds do not have a significant influence on capsule's bifurcation patterns but affect its progression in terms of fold crossing. To this end, numerical studies using path-following techniques implemented via the software COCO are performed. In this way, parameter-dependent families of periodic solutions of the capsule-fold model are studied, and critical points are detected to allow to develop control strategies for the capsule motion, in particular in order to cross certain types of circular folds by suitably varying its control parameters.

1. Introduction

The small intestine, a section of the gastrointestinal tract between the stomach and the colon, has been previously considered as an anatomical site inaccessible to gastroenterologists. Since the invention of capsule endoscopy two decades ago, it has become established as the primary modality for examining the surface lining of the small intestine [1–3]. However, its dependence on intestinal peristalsis for locomotion in the small intestine causes significant limitations. For example, its uncontrollable progression speed during the passage may lead to incomplete visualisation of the intestinal surface, and significant abnormalities could be missed. So, many researchers have been developing different robotic mechanisms for controllable capsule endoscopies, e.g., [4–6], and clinicians may examine the areas of interest carefully in real time. To reduce the trauma on the small intestine potentially caused by these mechanisms, e.g., [7], our present work aims to adapt the vibro-impact self-propulsion technique [8,9] into capsule endoscopy, and to explore the feasibility of

* Corresponding author.
E-mail addresses: y.yan@uestc.edu.cn (Y. Yan), zhangbaoquan1997@std.uestc.edu.cn (B. Zhang), jpaez@espol.edu.ec (J. Páez Chávez), y.liu2@exeter.ac.uk (Y. Liu).

https://doi.org/10.1016/j.cnsns.2022.106696

innovation for the next generation of endoscopy, i.e., the vibro-impact self-propelled capsule robot [10]. To achieve this, in the present paper, we will optimise the locomotion of such a robot in the small intestine with a further consideration of intestinal anatomy. With this study in place, we will be able to refine our prototype design [11] and develop a proper control strategy for controlling its locomotion in the intestinal environment.

Understanding the anatomy of the small intestine [12] is critical for improving the performance of the self-propelled capsule robot. Adult's small intestine has an average length of 6 [m] and a diameter of 3.5 [cm], which includes 0.25 [m] for the duodenum, 2.5 [m] for the jejunum, and 3.25 [m] for the ileum at its proximal, middle, and distal sections, respectively [13]. Mucosa in these sections is highly folded to slow down food passage and to absorb nutrients [14]. Thus, the self-propelled capsule robot moving in these sections for endoscopic diagnosis will engage with various circular folds to resist its progression. To this end, the model used in our previous studies, e.g., [15–17], which only considered the hoop stress introduced by the small intestine, should be further extended. The effect of the circular fold was observed in our previous experimental study [18], showing a sharp increase in the resistant force during the crossing procedure. To analytically revealing the capsule-fold interaction, an earlier work performed by Sliker et al. [19] assumed the maximum resistant force showing up once the capsule's head presses the fold from the side and touches its tip. In many cases, this presumption is not necessarily true. In addition, Sliker's model cannot be applied to model the dynamic crossing of the capsule robot, since it only can predict the maximum resistant force of the circular fold. Therefore, to evaluate the performance of the self-propelled capsule moving in the small intestine with regard to its progression speed, Slicker's model should be generalised to cope with the capsule's dynamic model. Our concerns in the present paper are (1) to study the dynamics of the capsule robot when it encounters various circular folds and (2) to optimise its control parameters (e.g., the frequency and amplitude of excitation) for a successful crossing.

Since the vibro-impact capsule robot involves both friction and impact, it is considered as a piecewise-smooth dynamical system [20,21] from nonlinear systems' point of view. In order to gain a deeper insight into the capsule dynamics, this work includes a numerical investigation of the piecewise-smooth model using path-following techniques, implemented via the software COCO (short form of Computational Continuation Core [22]). This is an analysis and development platform for the numerical treatment of continuation problems using MATLAB, which covers, to a large extent, the functionality of classical continuation packages, such as AUTO [23] and MATCONT [24]. In particular, in this work we will make extensive use of the COCO-toolbox 'hspo', which implements a segment-specific discretisation strategy in the framework of multi-segment boundary-value problems, thus allowing the numerical continuation of periodic solutions for piecewise-smooth dynamical systems. In this way, we will be able to study parameter-dependent families of periodic solutions and detect critical points that will allow to develop control strategies for the capsule motion, in particular in order to cross certain types of circular folds by suitably varying the frequency and amplitude of excitation. This approach has been extensively used in previous works, for instance in [11,25], where the authors utilised path-following techniques to optimise the performance of a preliminary capsule model.

Early works on self-propelled locomotion systems driven by internal vibration and environmental friction can be found from [26]. Liu et al. [8] studied the first vibro-impact driven capsule system and its dynamic behaviour through mathematical modelling and bifurcation analysis. The system consists of a capsule shell which interacts with an internal mass driven by a sinusoidal excitation in the presence of an environmental friction. The study mainly focused on system's progression and energy efficiency with respect to different system parameters. Various friction models for the capsule system and capsule's dynamic behaviour were considered in [9], where bidirectional control of the system was achieved by varying its mass ratio between the capsule shell and the internal mass or by switching between coexisting attractors. Fang and Xu [27] studied the stick–slip effect of a vibration-driven system in the presence of Coulomb dry friction. They focused on investigating different types of transitions between the slip and the sticking motions due to sliding bifurcations in the system, and performed an optimisation for the best progression by utilising the sticking feature of the system. Nunuparov et al. [28] developed a capsule robot that consisted of a housing and an internal body, connecting with each other via a helical spring. Bidirectional motion of the robot on a rough horizontal plane was achieved by periodically driving its internal body via the pulse-width modulation. Zimmermann et al. [29] experimentally implemented the driving concept to a linear motor controlled by a periodically magnetic field with consideration of dry and viscous friction. In [30], Nguyen and co-workers studied the effect of various dry and isotropic friction levels on the progression and dynamic response of a vibro-impact locomotion system. Their results showed that different frictions may lead the system to either period-1 or chaotic motion. Chernousko [31] studied the two-dimensional motions of a multibody locomotion system carrying internal masses in the presence of dry friction between the system and a horizontal plane. Zhan et al. [32] also considered the planar locomotion of a vibration-driven system with dry friction from mathematical modelling point of view. Zhang et al. [33] presented a novel design and experimental investigation for a self-propelled capsule robot capable of planar locomotion by using an electromagnetic actuator with orientation control. Recently, Zarychta et al. [34] presented a new Fourier series based numerical method for open-loop control optimisation of piecewise-smooth dynamical systems, like the vibration-driven capsule system [35]. In [36], Liao et al. developed a new method for speed optimisation and reliability analysis of the self-propelled capsule robot [11], moving in an uncertain frictional environment by considering the varying friction coefficient between the robot and its supporting surface. The proposed method was validated through numerical simulation and experimental testing, which can be used for the mobile robots with multiple control objectives and constraints. To continue this work and take the intestinal anatomy into account, we will address a more realistic optimisation issue in the present work: how to operate the vibro-impact capsule robot in the presence of a circular fold?

To reveal the performance of the vibro-impact capsule robot interacting with a circular fold, this paper is organised as follows. Section 2 proposes a new model of the vibro-impact capsule moving on a small intestine substrate in the presence of a circular fold exerting a resistance force on the capsule. This force is then approximated by piecewise polynomials to accelerate numerical analysis. Next, bifurcation analysis is performed in Section 3, finding the complex dynamics of the robot when it is engaged with the circular fold. In Section 4, path-following techniques via the software COCO is introduced to directly optimise the capsule's performance on fold crossing. Finally, conclusions are drawn in Section 5.

2. Mathematical modelling of the capsule dynamics

2.1. Modelling of capsule–intestine interaction

Fig. 1 illustrates a vibro-impact capsule robot moving horizontally in the x-direction (rightwards) on the small intestine with a thickness of H [mm] in the presence of a circular fold. As can be seen from the figure, the capsule has a cylindrical body with a length of L [mm] and a radius of R [mm], which connects its hemispheric head and tail. Since the capsule is very rigid compared with the soft tissue, it is assumed that the deformation of the incompressible and isotropic tissue conforms to the capsule profile. To further simplify the model of capsule–intestine interaction, it is assumed that the capsule can only translate in the xoy plane without rotation [19]. Thus, the capsule in Fig. 1(b) does not tilt when it contacts the fold. As seen in Fig. 1(c) for the front view of cross section A-A, the capsule's gravity results in a penetration into the tissue substrate for a depth of $\delta_{\max}$ [mm] in the y-direction. In front of the capsule, the small intestine has a circular fold with a height of h [mm], a width of w [mm], and its centre located at $x = x_{\mathrm{b}}$ [mm]. Given this fold, the shape of the small intestine can be approximated by the following function [19]

$$f(x) = \begin{cases} h\cos\left(\frac{x-x_{\mathrm{b}}}{2w}\pi\right), & |x - x_{\mathrm{b}}| \le w, \\ 0, & |x - x_{\mathrm{b}}| > w. \end{cases} \tag{1}$$

A side view of cross section B-B for $x \in [x_{\mathrm{c}} - L - R, x_{\mathrm{c}} + R]$ is displayed in Fig. 1(d), where x_{c} is the location of capsule's head centre (or in other words, capsule's displacement), showing a round cross section of the capsule with a radius of

$$\rho(x) = \begin{cases} \sqrt{R^2 - (x - x_{\mathrm{c}})^2}, & x_{\mathrm{c}} < x \le x_{\mathrm{c}} + R, \\ R, & x_{\mathrm{c}} - L \le x \le x_{\mathrm{c}}, \\ \sqrt{R^2 - (x - x_{\mathrm{c}} + L)^2}, & x_{\mathrm{c}} - R - L \le x < x_{\mathrm{c}} - L. \end{cases} \tag{2}$$

Given Eq. (2) and the capsule's radius and penetration, one can obtain the vertical position of any given point of the capsule bottom displayed in Fig. 1(c) as

$$\begin{aligned} p(x) &= R - \delta_{\max} - \rho(x) \\ &= \begin{cases} R - \delta_{\max} - \sqrt{R^2 - (x - x_{\mathrm{c}})^2}, & x_{\mathrm{c}} < x \le x_{\mathrm{c}} + R, \\ -\delta_{\max}, & x_{\mathrm{c}} - L \le x \le x_{\mathrm{c}}, \\ R - \delta_{\max} - \sqrt{R^2 - (x - x_{\mathrm{c}} + L)^2}, & x_{\mathrm{c}} - R - L \le x < x_{\mathrm{c}} - L. \end{cases} \end{aligned} \tag{3}$$

For a given position, Fig. 1(d) shows the vertical distance from the capsule's central axis to the tissue surface as

$$d(x) = R - \delta_{\max} - f(x). \tag{4}$$

When the distance is larger than the radius of the section, $d(x) > \rho(x)$, there is no capsule–intestine interaction. On the contrary, they have a limited contact angle, $\theta \in [-\alpha(x), \alpha(x)]$ for $d(x) \le \rho(x)$, where $\alpha(x)$ is the limit given by

$$\alpha(x, \delta_{\max}) = \cos^{-1}\left(\min\left(1, \frac{d(x)}{\rho(x)}\right)\right). \tag{5}$$

Given the contact angle, the shape function of the capsule bottom displayed in Fig. 1(d) is revised to be

$$p(x, \theta) = R - \delta_{\max} - \rho(x)\cos(\theta), \tag{6}$$

which is compatible with Eq. (3) as $p(x, 0) = p(x)$. As seen in Fig. 1(d), $p(x, \theta)$ represents the vertical position of any given point of the capsule bottom.

Wherever the tissue conforms to the capsule profile, the small intestine deforms from its own shape function, $f(x)$, to the capsule's shape function, $p(x, \theta)$, yielding the deformation

$$\delta(x, \theta) = \max\left(0, f(x) - p(x, \theta)\right). \tag{7}$$

Dividing the deformation by the original thickness of the substrate yields the tissue strain

$$\epsilon(x, \theta) = \frac{\delta(x, \theta)}{H + f(x)}. \tag{8}$$

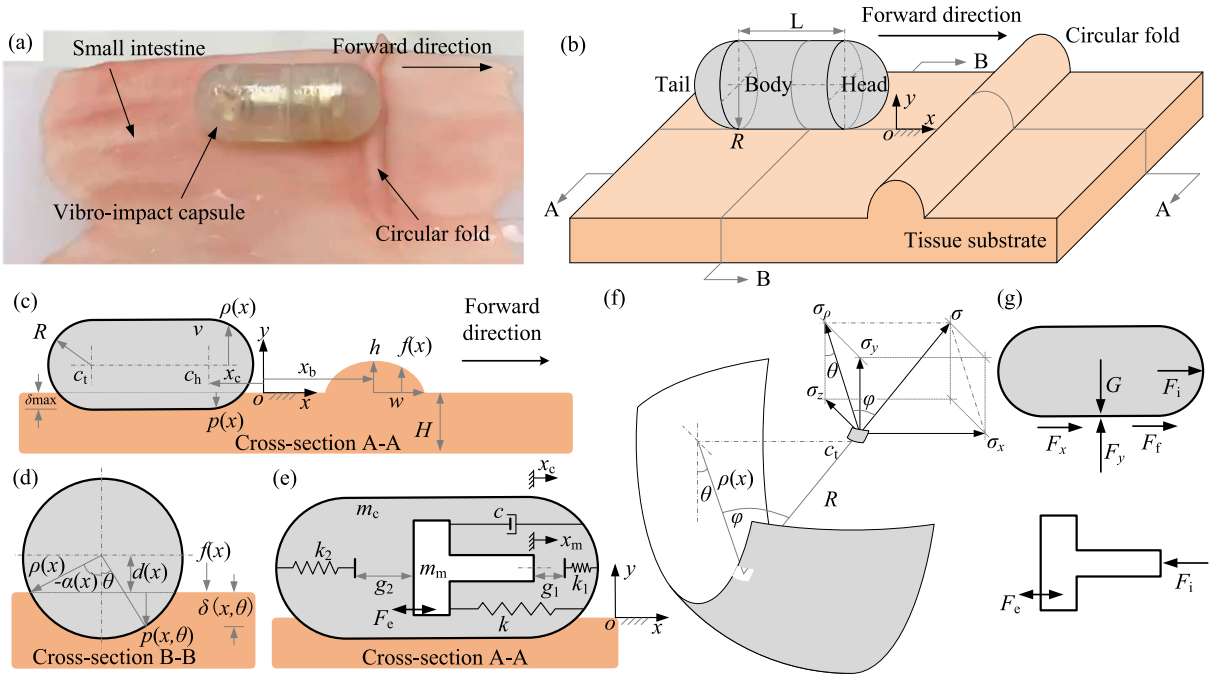

Fig. 1. (a) Photograph and (b) schematic of a vibro-impact capsule robot moving rightwards on a piece of small intestine in the presence of a circular fold. Geometries of the capsule and the circular fold are displayed in (c) the cross section A-A and (d) the cross section B-B of Fig. 1(b). It is assumed that the capsule can translate only without any rotation. (e) The capsule robot has an inner mass driven by an external excitation which interacts with the capsule shell via a primary spring, a damper and two impact constraints. (f) The contact surface between the small intestine (including the fold) and the capsule shell, and the small intestine exerts pressure on the capsule shell via this surface. (g) Free-body diagrams of the capsule and the inner mass.

The strain is then multiplied by the Young's module of the tissue, E, for the stress

$$\sigma(x,\theta) = \epsilon(x,\theta)E(x). \tag{9}$$

It is seen in Fig. 1(f) that the stress exerts normal pressure on the capsule shell, which is mapped onto $x-$ and $y-$axes as

$$\begin{aligned} \sigma_x(x,\theta) &= \sigma(x,\theta)\sin(\varphi), \\ \sigma_y(x,\theta) &= \sigma(x,\theta)\cos(\varphi)\cos(\theta), \end{aligned} \tag{10}$$

where

$$\varphi(x) = \begin{cases} -\sin^{-1}\left(\frac{x-x_c}{R}\right), & x_c < x \le x_c + R, \\ 0, & x_c - L \le x \le x_c, \\ -\sin^{-1}\left(\frac{x-x_c+L}{R}\right), & x_c - R - L \le x < x_c - L, \end{cases} \tag{11}$$

is the angle of anticlockwise rotation from R to $\rho(x)$.

Integrating $\sigma_y(x,\theta)$ over the capsule shell yields the vertical reaction force exerted by the tissue on the capsule as

$$F_y(x_c,\delta_{\max}) = \int_{x_c-L-R}^{x_c+R}\int_{-\alpha(x,\delta_{\max})}^{\alpha(x,\delta_{\max})} \sigma_y(x,\theta)\rho(x)\mathrm{d}\theta\frac{\mathrm{d}x}{\cos(\varphi(x))}. \tag{12}$$

From the free body diagram of the capsule shell in Fig. 1(g), one can see that the vertical force cancels the capsule gravity by

$$F_y(x_c,\delta_{\max}) = G, \tag{13}$$

which implicitly determines the penetration depth, $\delta_{\max}$, for a given position, x_c. Namely, $\delta_{\max}(x_c)$ is an implicit function of x_c. Next, integrating $\sigma_x(x,\theta)$ yields the horizontal reaction force as

$$F_x(x_c) = \int_{x_c-L-R}^{x_c+R}\int_{-\alpha(x,\delta_{\max}(x_c))}^{\alpha(x,\delta_{\max}(x_c))} \sigma_x(x,\theta)\rho(x)\mathrm{d}\theta\frac{\mathrm{d}x}{\cos(\varphi(x))}. \tag{14}$$

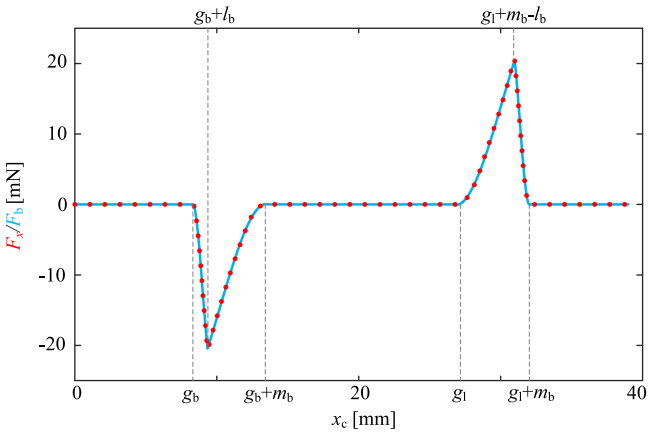

Fig. 2. Horizontal reaction force (red dots), $F_x(x_c)$, and its approximation (blue solid), $F_b(x_c)$ for $R = 5.5$ [mm], $L = 15$ [mm], $m_m = 1.8$ [g], $m_c = 1.67$ [g], $E = 25$ [kPa], $H = 0.69$ [mm], $x_b = 12.66$ [mm], $h = 1.6$ [mm], and $w = 1.665$ [mm], which corresponds with the approximating parameters of $g_b = 8.31$ [mm], $l_b = 1.033$ [mm], $m_b = 5.31$ [mm], $g_l = 26.71$ [mm], $\beta_0 = -0.09111$ [mN/mm], $\beta_1 = 39.18$ [mN/mm^2], $\beta_2 = -19.25$ [mN/mm^3], $\eta_0 = 0.6945$ [mN/mm], $\eta_1 = 2.183$ [mN/mm^2], $\beta_2 = 0.2106$ [mN/mm^3].

To study the capsule dynamics, one should continuously solve Eq. (13) for δ_{max} by numerical iteration and numerically integrate Eq. (14) for F_x, which are very computationally expensive. Alternatively, one can solve Eq. (14) for a given group of parameters beforehand, and approximate it by using a piecewise function written as

$$\begin{aligned} F_b(x_c) = & -(H(x_c - g_b) - H(x_c - (g_b + l_b)))F_{b1}(x_c) \\ & -(H(x_c - (g_b + l_b)) - H(x_c - (g_b + m_b)))F_{b2}(x_c) \\ & +(H(x_c - g_\ell) - H(x_c - (g_\ell + m_b - l_b)))F_{b3}(x_c) \\ & +(H(x_c - (g_\ell + m_b - l_b)) - H(x_c - (g_\ell + m_b)))F_{b4}(x_c) \end{aligned} \tag{15}$$

where

$$\begin{aligned} F_{b1}(x_c) &= \beta_0(x_c - g_b) + \beta_1(x_c - g_b)^2 + \beta_2(x_c - g_b)^3, \\ F_{b2}(x_c) &= \eta_0(x_c - (g_b + m_b)) + \eta_1(x_c - (g_b + m_b))^2 + \eta_2(x_c - (g_b + m_b))^3, \\ F_{b3}(x_c) &= -\eta_0(x_c - g_\ell) + \eta_1(x_c - g_\ell)^2 - \eta_2(x_c - g_\ell)^3, \\ F_{b4}(x_c) &= -\beta_0(x_c - (g_\ell + m_b)) + \beta_1(x_c - (g_\ell + m_b))^2 - \beta_2(x_c - (g_\ell + m_b))^3, \end{aligned}$$

where $H(\cdot)$ stands for the Heaviside step function. As an example, the approximation by Eq. (15) shown in Fig. 2 matches perfectly with the resistance force obtained by Eq. (14). There are 4 turning points marked in Fig. 2, g_b, $g_b + m_b$, g_l, and $g_l + m_b$. The capsule head starts to contact the fold when $x_c \geq g_b$ to climb up, and stays on the top of the fold when $x_c \in [g_b + m_b, g_l]$. For $x_c \in [g_l, g_l + m_b]$, the capsule climbs down the fold with its tail engaged with the fold.

2.2. Model of the vibro-impact capsule

As displayed in Fig. 1(e), the capsule's shell has a mass m_c [g], inside of which there is a magnet of mass m_m [g]. Compared with Fig. 1(g), one can see that the capsule's gravity involves both of the inner mass and the shell, i.e., $G = (m_m + m_c)\,g$, where $g = 9810$ [mm/s^2] is the gravitational acceleration. The magnetic inner mass is connected to the capsule shell via a damped spring, which has stiffness k [N/m] and damping c [Ns/m]. Besides, there are two extra springs in front of and behind the magnet to constrain its motion. They have stiffness, k_1 [N/m] and k_2 [N/m], and gaps, g_1 [mm] and g_2 [mm].

The magnetic inner mass is periodically driven by a sinusoid external excitation written as

$$F_e = A\sin(\Omega t), \tag{16}$$

where A and Ω are the amplitude and frequency of the excitation, respectively. Through the damper and springs, the inner mass interacts with the capsule shell by the following piecewise linear interactive force

$$F_i = \begin{cases} kx_r + cv_r + k_1\left(x_r - g_1\right), & \text{if } x_r > g_1, \\ kx_r + cv_r, & \text{if } -g_2 \leq x_r \leq g_1, \\ kx_r + cv_r + k_2\left(x_r + g_2\right), & \text{if } x_r < -g_2, \end{cases} \tag{17}$$

Table 1
Parameters of the capsule and the small intestine [11,18].

Parameter	Symbol	Unit	Value
Capsule radius	R	mm	5.50
Capsule length	L	mm	15
Damping	c	Ns/m	0.0156
Right gap	g_1	mm	1.6
Left gap	g_2	mm	0
Stiffness of the primary spring	k	N/m	62
Stiffness of the second spring	k_1	N/m	27900
Stiffness of the tertiary spring	k_2	N/m	53500
Mass of the magnet (inner mass)	m_m	g	1.8
Mass of the capsule	m_c	g	1.67
Young's Modulus of the small intestine	E	kPa	10
Frictional coefficient	μ	–	0.2293
Thickness of the small intestine	H	mm	0.69

Table 2
Parameters of various circular folds [18].

Parameter	Symbol	Unit	Case 1	Case 2	Case 3	Case 4	Case 5
Location	x_b	mm	12.66	12.66	12.66	12.66	12.66
Height	h	mm	0	1.6	1.6	2.347	2.347
Width	w	mm	0	1.665	1.665	1.545	1.545
Young's Modulus	E	kPa	0	10	25	10	25

where $x_\mathrm{r} = x_\mathrm{m} - x_\mathrm{c}$ and $v_\mathrm{r} = \dot{x}_\mathrm{m} - \dot{x}_\mathrm{c}$ are the relative displacement and velocity between the magnet and the capsule shell.

Driven by F_i, the capsule shell may move either forward or backward, which is subjected to the reaction from the small intestine including F_x and Coulomb friction, F_f [mN]. Depending on the moving speed and the other forces, the frictional force is given by

$$F_\mathrm{f} = \begin{cases} -\operatorname{sign}(\dot{x}_\mathrm{c})\mu G, & \text{if } \dot{x}_\mathrm{c} \neq 0, \\ -\operatorname{sign}(F_\mathrm{i} + F_\mathrm{x})\mu G, & \text{if } \dot{x}_\mathrm{c} = 0 \text{ and } \operatorname{abs}(F_\mathrm{i} + F_\mathrm{x}) \geq \mu G, \\ -F_\mathrm{i} - F_\mathrm{x}, & \text{if } \dot{x}_\mathrm{c} = 0 \text{ and } \operatorname{abs}(F_\mathrm{i} + F_\mathrm{x}) < \mu G, \end{cases} \tag{18}$$

where sign$(*)$ and abs$(*)$ return the sign and absolute value of $*$, respectively, and μ is the frictional coefficient. Given all of the forces and free-body diagram in Fig. 1(g), the governing equation of the capsule robot can be written as

$$\begin{cases} m_\mathrm{m}\ddot{x}_\mathrm{m} = F_\mathrm{e} - F_\mathrm{i}, \\ m_\mathrm{c}\ddot{x}_\mathrm{c} = F_\mathrm{i} + F_x + F_\mathrm{f}. \end{cases} \tag{19}$$

3. Simulation and bifurcation analysis

With the model proposed in Eq. (19), the capsule dynamics will be numerically investigated. In addition, default values of the capsule and capsule–intestine interaction are listed in Tables 1 and 2, which were borrowed from our previous experimental- studies [11,18]. In detail, for various circular folds listed in Table 2, Case 1 is for flat intestine substrate without any fold, and Case 2 is for a small fold with a small elasticity. Compared with Case 2, Cases 3 and 5 have a larger Young's modulus indicating a harder fold, while Case 4 considers a sharper fold, i.e., a larger height and a smaller width.

Next, Rung–Kutta method was used for numerical integration with Eq. (19), with the transient phase skipped and the steady state kept for bifurcation analysis. To construct the bifurcation diagram, zero initial conditions, $(x_\mathrm{m}, \dot{x}_\mathrm{m}, x_\mathrm{c}, \dot{x}_\mathrm{c}) = (0, 0, 0, 0)$, was firstly used. Then both of backward and forward sweeping of bifurcation parameters were locally performed for coexisting attractors. Finally, the relative magnet-capsule velocity v_r was recorded for every excitation period, which was plotted as functions of the excitation amplitude A. In the bifurcation diagrams displayed in this section, red, blue, and green dots will be successively used to represent the coexisting attractors. Besides, the corresponding trajectories on the phase plane $(x_\mathrm{r}, v_\mathrm{r})$ are marked by P-l-m-n to indicate a period-l motion of the capsule with m back and n front impacts on the constraints.

Bifurcation diagrams for different cases of circular folds by using excitation amplitude as a branching parameter are displayed in Fig. 3, where excitation frequency was calculated at $\Omega = 35$ [Hz] and the rest parameters were given in Table 1. As can be seen from the figure, the capsule shows very similar dynamic responses no matter which fold is considered. However, the background colour that denotes different motions of the capsule in Fig. 3(a) is very different from the others, which only has red and green regions for backward and forward progression, without any engagement with the fold. By contrast, the cases in Figs. 3(b-e) introduce two special states that the capsule's forward and backward

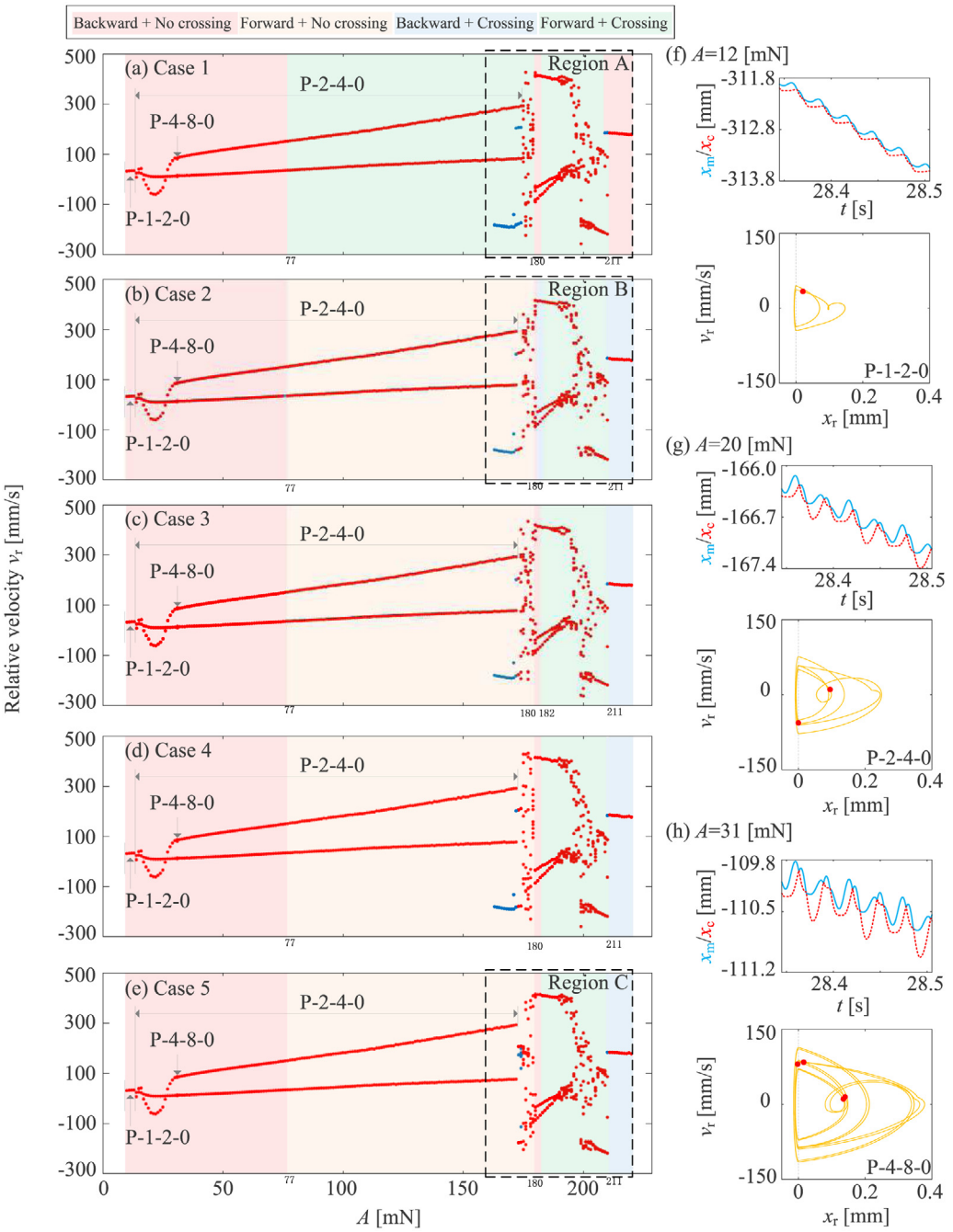

Fig. 3. Bifurcation diagrams for (a) Case 1, (b) Case 2, (c) Case 3, (d) Case 4, and (e) Case 5 by varying the amplitude of excitation A [mN] calculated for $\Omega = 35$ [Hz] and the rest parameters were adopted from Table 1. Despite different fold parameters were employed, the capsule had backward motions without any contact with the circular fold for $A \leq 77$ [mN], performing the similar dynamics as illustrated in panels (f–h).

motions (indicated by yellow and blue, respectively) are stopped by the fold, and the capsule oscillates without any progression.

For $A < 77$ [mN], as seen in Figs. 3(a–e), all of them have a red background, indicating backward motion without contacting the fold on its right side. Since the fold does not play a role in the capsule dynamics, all of the 5 cases display identical response, which is P-1-2-0 for $A \leq 12$ [mN] where it undergoes periodic doubling to be P-2-4-0. Then, another periodic doubling bifurcation occurs for $A = 31$ [mN] to yield P-4-8-0 motion, which immediately changes back into P-2-4-0 thereafter. As seen in Figs. 3(b-e), the capsule starts to move forward for $A > 77$ [mN], but the motion is not

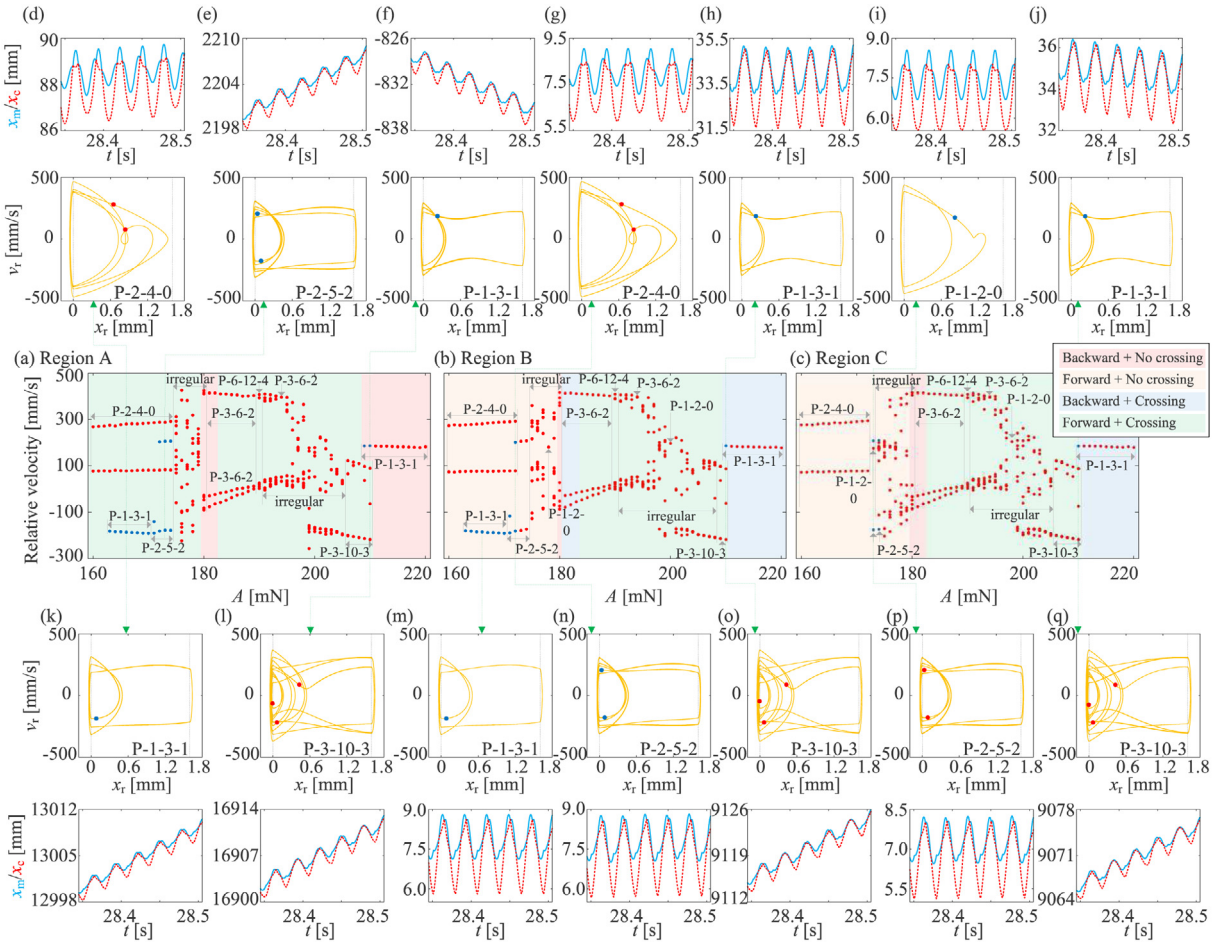

Fig. 4. Regions A-C corresponding with Cases 1, 2, and 5 in Fig. 3 are enlarged in Panels (a-c), with the time series and phase portraits for typical periodic motions plotted. More specifically, Panels (d, k) $A = 166$ [mN], (e) $A = 173$ [mN] and (f, l) $A = 210$ [mN] are for Case 1, Panels (m) $A = 166$ [mN], (g, n) $A = 172$ [mN] and (h, o) $A = 210$ [mN] are for Case 2, and Panels (i, p) $A = 173$ [mN] and (j, q) $A = 210$ [mN] are for Case 5.

strong enough to cross any folds. The trend of forward motion is temporarily changed into backward for $A \in [180, 182]$ [mN]. Then the capsule moves forward again, which is strong enough to cross the fold for $A \in (182, 211]$ [mN]. For $A > 211$ [mN], backward motion shows up again, but it is stopped by the fold, since the capsule has already crosses the fold during the transient phase.

To clarify the influence of folds on the capsule dynamics, Regions A-C marked in Figs. 3(a–b) and (e) are enlarged in Fig. 4. There is no difference in the bifurcation pattern for $A \in [183, 210]$, where the capsule keeps progressing forward no matter there is a fold or not. More specifically, P-3-6-2 motion is observed for $A \geq 183$ [mN], which undergoes a periodic doubling bifurcation to be P-6-12-2 for $A = 190$ [mN]. This motion immediately changes into irregular for further increase of the excitation amplitude, except a window of P-3-6-2 motion for $A = 194$ [mN]. The irregular motion becomes P-3-10-3 for $A > 205$ [mN], which lasts until A becomes larger than 210 [mN]. In Fig. 4(a) for Case 1, the P-2-4-0 forward motion coexists with P-1-3-1 forward motion (blue dots) for $A \in [163, 170]$ [mN], and the P-1-3-1 motion undergoes periodic doubling to be P-2-5-2 for $A \in [171, 174]$ [mN]. Both of the P-2-4-0 and P-2-5-2 motions disappear for $A > 174$ [mN], where the capsule motion keeps irregular before the backward progression shows up for $A \geq 180$ [mN].

Compared with Fig. 4(a), Fig. 4(b) for Case 2 displays a very similar bifurcation pattern, but the forward motion for $A < 180$ [mN] is stopped by the fold. For Case 3 in Fig. 4(c), by contrast, the coexisting P-1-3-1 for $A \in [163, 170]$ disappears. In addition, the fold in Case 5 is much harder to be crossed in the transient phase, so that the blue background for $A \in [181, 183]$ [mN] in Fig. 4(b) becomes red. This phenomenon is clearly illustrated in Fig. 5, where all of the phase portraits in Figs. 5(a-c) are P-3-6-2 and have no crucial difference, but the progressive motion in Figs. 5(d–m) are quite different from each other. The phase portrait in Fig. 5(a) for $A = 181$ [mN] corresponds with Cases 1, and 3–5, showing a steady state of backward motion. Compared with the small soft fold for Case 3 in Fig. 5(f), Case 5 for a large hard fold in Fig. 5(h) has a shorter transient phase of capsule-fold contact. Specially for Case 2 in Fig. 5(b), the softest and smallest fold is crossed by the capsule during the transient phase, but it stops the capsule's steady backward progression. For $A = 184$

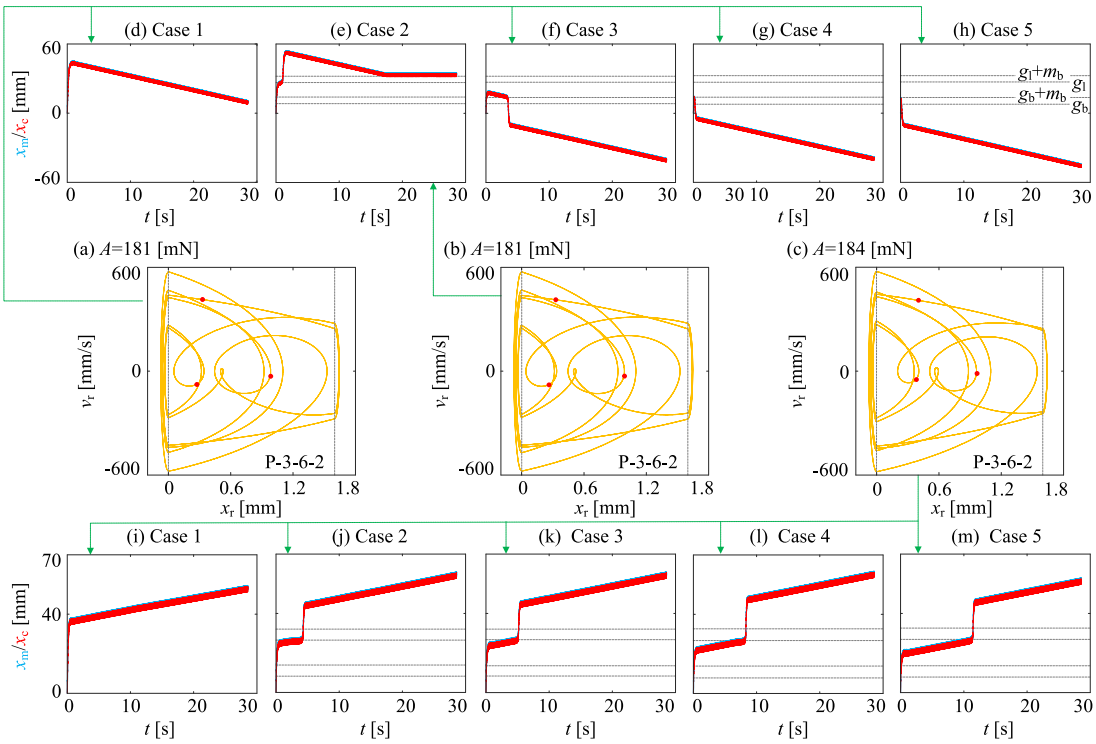

Fig. 5. Phase portraits for $\Omega = 35$ [Hz] and (a) $A = 181$ [mN], (b) $A = 181$ [mN], and (c) $A = 184$ [mN], where Panel (a) corresponds with Cases 1, and 3–5 in Panels (d, f–h), Panel (b) corresponds with Case 2 in Panel (e), and Panel (c) corresponds with Cases 1–5 in Panels (i–m).

[mN], as seen in Figs. 5(i–m), the P-3-6-2 motion always progresses forward, but a larger and harder fold requires a longer time to be crossed.

For $\Omega = 45$ [Hz], the bifurcation diagrams for Cases 5, 1, and 2 are displayed in Figs. 6(a) and 7. They still share the same bifurcation pattern in the red regions, and have similar dynamic properties in the others. In the red region, the capsule motion is P-2-3-0 for $A \in [10, 15]$, which undergoes periodic doubling to be P-4-6-0 for $A \in [16, 19]$. It then undergoes a cascade of reverse periodic doubling to be P-2-3-0 for $A = 20$ [mN] and P-1-1-0 for $A \in [21, 45]$ [mN]. Except the irregular motion for $A = 48$ [mN], it is then undergoes a cascade of periodic doubling to be P-2-3-0 for $A \in [46, 77]$ [mN] and P-4-6-0 for $A \in [78, 45]$ [mN]. The response becomes irregular for $A \in [78, 127]$ [mN], scattered with several windows of P-1-1-0 motion. In addition, there coexists another backward progression of P-3-5-0 motion (green dots) for $A > 106$ [mN], which lasts until $A > 138$ [mN]. Finally, another red region shows up for $A \in [205, 209]$ for P-2-4-2 motion.

Except the capsule dynamics located in the red regions, the other responses in Fig. 6 for Case 5 are all in the yellow region which corresponds with a forward progression stopped by the fold. It is P-1-2-1 (blue dots) for $A \in [101, 111]$ [mN], which changes into P-3-6-2 (blue dots) for $A \in [112, 129]$ [mN]. The two responses coexist with the backward progression of irregular, P-1-1-0 and P-3-5-0 responses discussed above. Before the disappearance of P-3-6-2 motion for $A = 129$ [mN], P-2-4-1 for $A \in [134, 175]$ [mN] with P-4-8-2 motion scattered shows up. Moreover, there coexists an irregular motion (blue dots) for $A \geq 173$ [mN], which lasts for $A \leq 204$ [mN]. Finally, the response becomes P-1-2-1 for $A > 204$ [mN], with backward P-2-4-2 motion (blue dots) coexisting for $A \in [204, 209]$ [mN]. To further illustrate the regularity of the typical capsule dynamics in Fig. 6, power spectrum density (PSD) of the capsule velocity is illustrated as well. It is seen that all of the periodic motions in Figs. 6(b), (d) and (f–k) have sharp peaks at the driven frequency, $\Omega = 45$ [Hz], and its sub- and super-harmonics, with ignorable power for any other frequencies. By contrast, the PSD in Figs. 6(c) and (e) illustrates that the irregular motions have their energy distributed in a wide frequency region. Compared with Fig. 6(a) for Case 5, Fig. 7(a) for Case 1 has the whole yellow region changed into green for a forward progression since no fold can stop the capsule. By contrast, Fig. 7(b) for Case 2 (small soft fold) can stop most forward progressions of the capsule, but P-1-2-1 for large excitation amplitude still can cross this fold.

The bifurcation pattern for an excitation frequency of 55 [Hz], as displayed in Fig. 8 becomes much simpler compared with those of $\Omega = 35$ [Hz] and 45 [Hz]. As seen, the capsule normally performs a backward progression for $A \in [10, 220]$ [mN], except the coexisting forward progression for large excitation amplitude. Moreover, the majority of the backward motion is P-1-1-0, except the P-3-4-0 motion for $A \in [10, 14]$ [mN] and the irregular motion for $A \in [16, 20]$ [mN]. Roughly for $A > 150$ [mN], There exists P-1-2-1 forward motion (blue dots), which undergoes periodic doubling to be

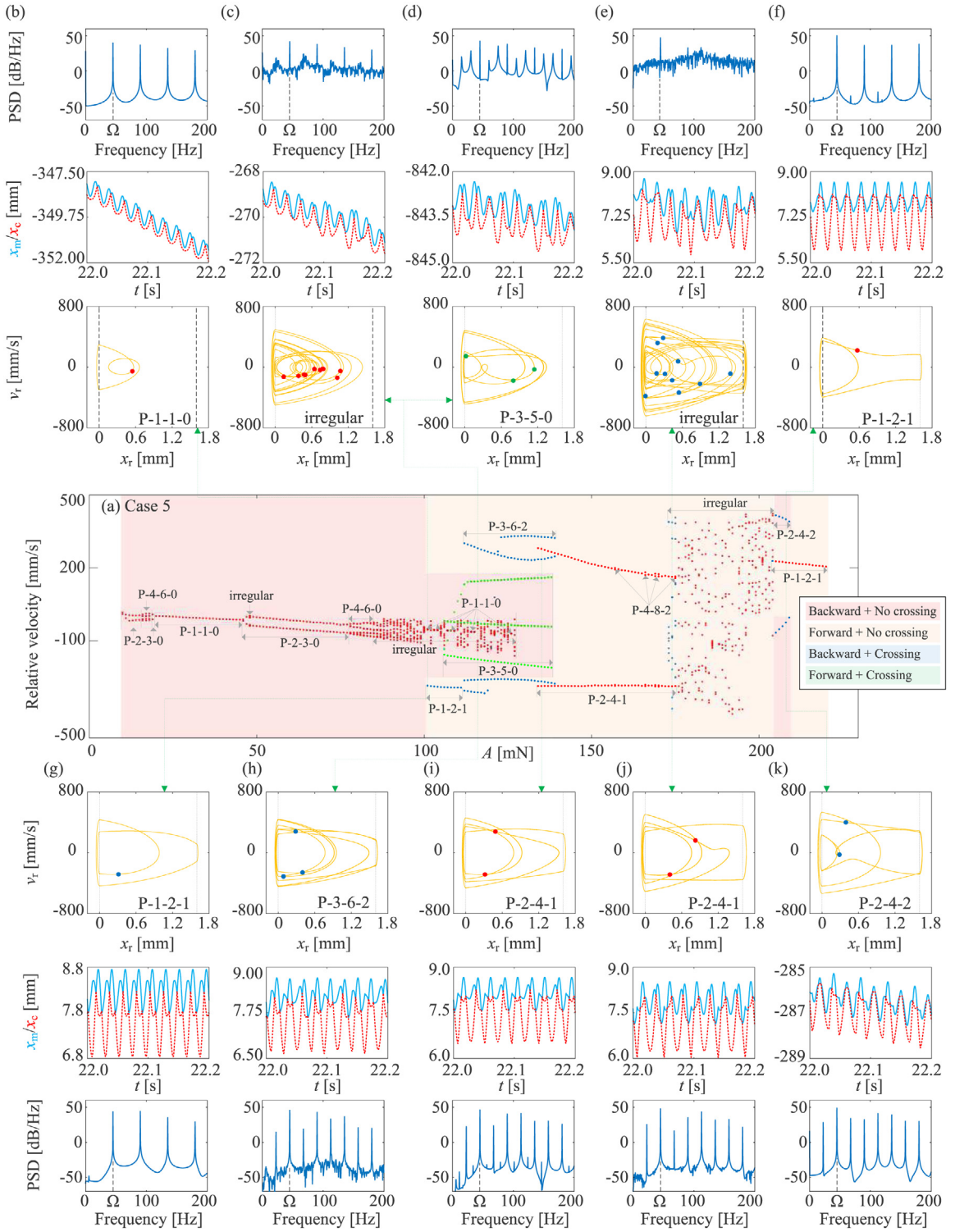

Fig. 6. (a) Bifurcation diagram for $\Omega = 45$ [Hz] and Case 5, with power spectrum density, time series and phase portraits for (b, g) $A = 101$ [mN], (c, d, h) $A = 116$ [mN], (i) $A = 135$ [mN], (e, j) $A = 174$ [mN], and (f, k) $A = 208$ [mN] displayed.

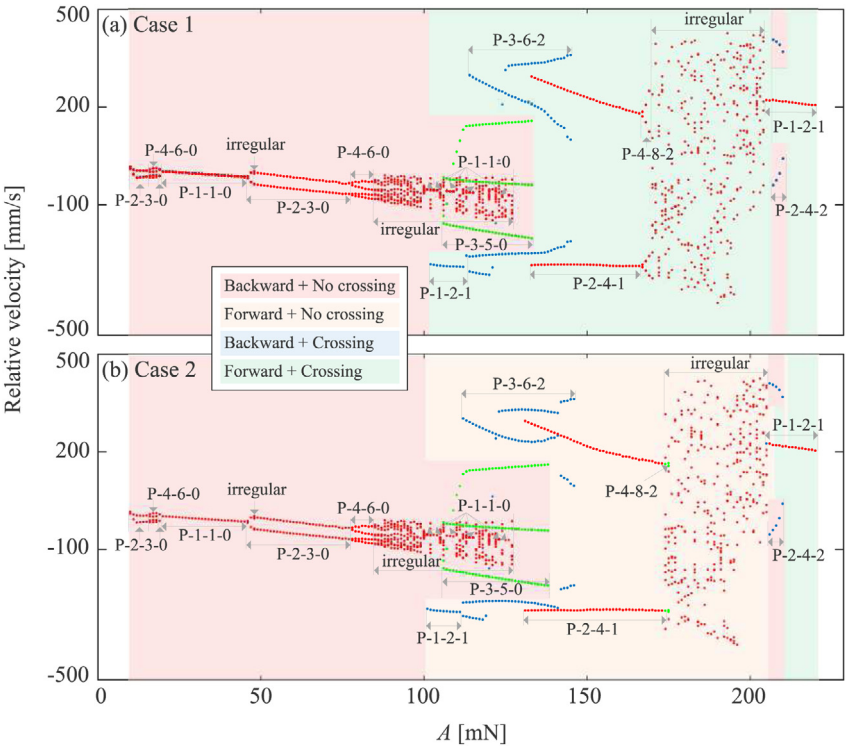

Fig. 7. Bifurcation diagrams for $\Omega = 45$ [Hz], and (a) Case 1 and (b) Case 2.

P-2-4-2 (blue dots) for $A \approx 200$ [mN]. Except in Fig. 8(a) for Case 1, this forward progression is stopped by either the small and soft or the large and hard folds for Cases 2 and 5 as shown in Figs. 8(b–c).

4. Numerical study of the capsule system using path-following methods

4.1. Mathematical formulation for path-following analysis

For the numerical analysis of the capsule system (19), it is convenient to consider the following nondimensional parameters and variables:

$$
\begin{array}{lllll}
\Omega_0 = \sqrt{\dfrac{k}{m_{\mathrm{m}}}}, & \tau = \Omega_0 t, & \omega = \dfrac{\Omega}{\Omega_0}, & \xi = \dfrac{c}{2m_{\mathrm{m}}\Omega_0}, & \alpha_a = \dfrac{A}{\mu G}, \\
\widetilde{x}_{\mathrm{m}} = \dfrac{k}{\mu G}x_{\mathrm{m}}, & \widetilde{x}_{\mathrm{c}} = \dfrac{k}{\mu G}x_{\mathrm{c}}, & \widetilde{x}_{\mathrm{r}} = \dfrac{k}{\mu G}x_{\mathrm{r}}, & \widetilde{g}_1 = \dfrac{k}{\mu G}g_1, & \widetilde{g}_2 = \dfrac{k}{\mu G}g_2, \\
\widetilde{g}_{\mathrm{b}} = \dfrac{k}{\mu G}g_{\mathrm{b}}, & \widetilde{l}_{\mathrm{b}} = \dfrac{k}{\mu G}l_{\mathrm{b}}, & \widetilde{g}_{\ell} = \dfrac{k}{\mu G}g_{\ell}, & \widetilde{m}_{\mathrm{b}} = \dfrac{k}{\mu G}m_{\mathrm{b}}, & \gamma = \dfrac{m_{\mathrm{m}}}{m_{\mathrm{c}}}, \\
\widetilde{k}_1 = \dfrac{k_1}{k}, & \widetilde{k}_2 = \dfrac{k_2}{k}, & \widetilde{\beta}_0 = \dfrac{\beta_0}{k}, & \widetilde{\beta}_1 = \dfrac{\beta_1 \mu G}{k^2}, & \widetilde{\beta}_2 = \dfrac{\beta_2(\mu G)^2}{k^3}, \\
\widetilde{\eta}_0 = \dfrac{\eta_0}{k}, & \widetilde{\eta}_1 = \dfrac{\eta_1 \mu G}{k^2}, & \widetilde{\eta}_2 = \dfrac{\eta_2(\mu G)^2}{k^3}. &&
\end{array}
\tag{20}
$$

Considering these nondimensional parameters, we also introduce the function

$$\widetilde{F}_{\mathrm{b}}(\widetilde{x}_{\mathrm{c}}) = \frac{1}{\mu G} F_{\mathrm{b}}\left(\frac{\mu G}{k}\widetilde{x}_{\mathrm{c}}\right),$$

which represents the nondimensional restoring force when the capsule hits a fold. In what follows, we will denote by $z = (x_{\mathrm{m}}, v_{\mathrm{m}}, x_{\mathrm{r}}, v_{\mathrm{r}})^T \in \mathbb{R}^4$ and $\lambda = (\omega, \alpha_a, \gamma, k_1, k_2, \xi, g_1, g_2, g_{\mathrm{b}}, l_{\mathrm{b}}, g_{\ell}, m_{\mathrm{b}}, \beta_0, \beta_1, \beta_2, \eta_0, \eta_1, \eta_2) \in \times\mathbb{R}^{18}$ the state variables and parameters of the system, respectively, where the tildes have been dropped for the sake of simplicity. In

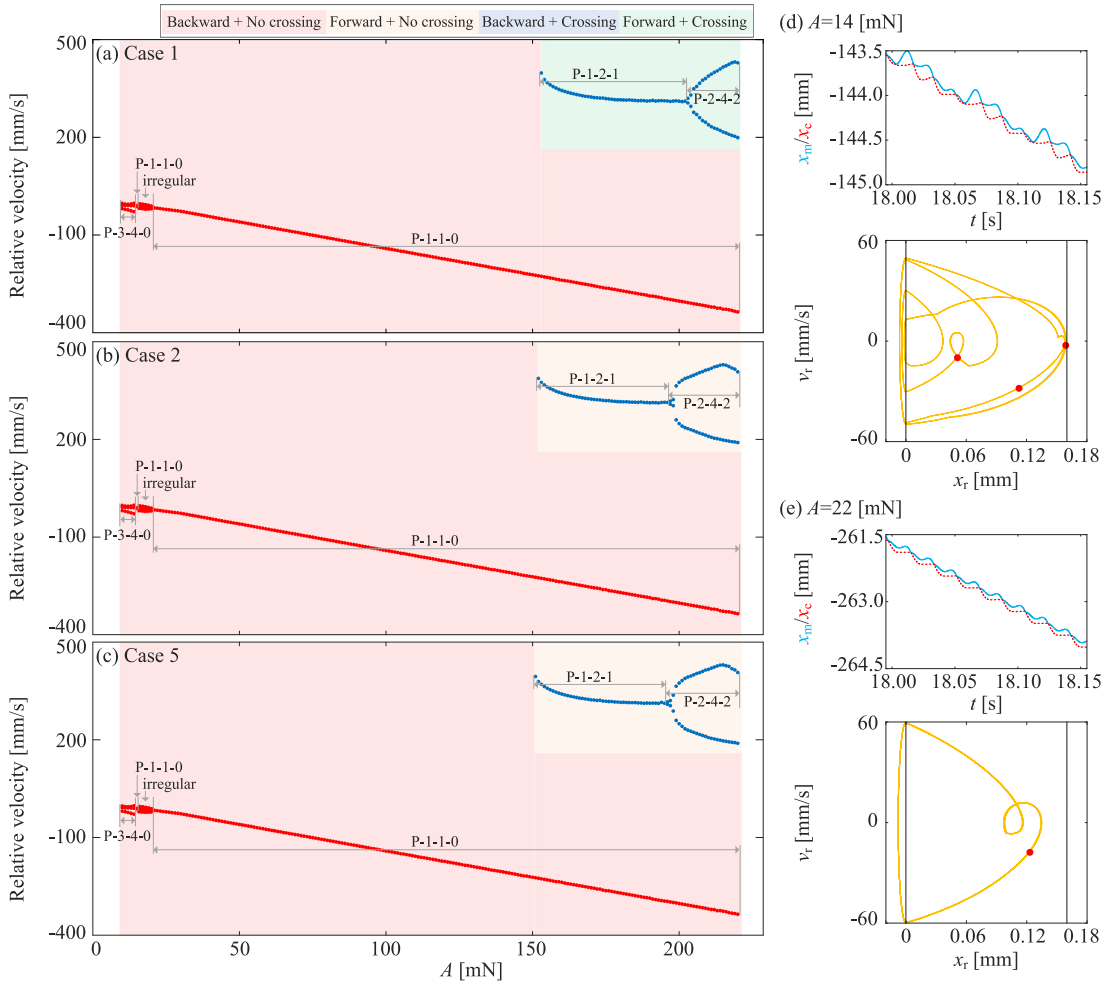

Fig. 8. Bifurcation diagrams for $\Omega = 55$ [Hz], and (a) Case 1, (b) Case 2 and (c) Case 5, with the times series and phase portraits for (d) $A = 14$ [mN] and (e) $A = 22$ [mN] showing their backward motions.

this framework, the capsule motion can be described by the equation (cf. (19))

$$z' = \begin{pmatrix} v_{\mathrm{m}} \\ \alpha_a \sin(\omega\tau) - f_0 - H_{\mathrm{k}_1} f_1 - H_{\mathrm{k}_2} f_2 \\ v_{\mathrm{r}} \\ \alpha_a \sin(\omega\tau) - f_0 - H_{\mathrm{k}_1} f_1 - H_{\mathrm{k}_2} f_2 - \gamma \left| H_{\mathrm{vel}} \right| \left(f_0 + H_{\mathrm{k}_1} f_1 + H_{\mathrm{k}_2} f_2 + H_{\mathrm{fold}} F_{\mathrm{b}}(x_{\mathrm{c}}) - H_{\mathrm{vel}} \right) \end{pmatrix} = f_{\mathrm{CAP}}(z, \lambda, H_{\mathrm{k}_1}, H_{\mathrm{k}_2}, H_{\mathrm{vel}}, H_{\mathrm{fold}}), \tag{21}$$

where the prime symbol denotes derivative with respect to the nondimensional time τ and $f_0 = x_{\mathrm{r}} + 2\xi v_{\mathrm{r}}$, $f_1 = k_1(x_{\mathrm{r}} - g_1)$, $f_2 = k_2(x_{\mathrm{r}} + g_2)$. Furthermore, the symbols H_{k_1}, H_{k_2}, H_{vel}, and H_{fold} are discrete variables defining the operation modes of the system, according to the rules

$$H_{\mathrm{k}_1} = \begin{cases} 1, & x_{\mathrm{r}} - g_1 \geq 0, \quad \text{(contact with } k_1\text{)}, \\ 0, & x_{\mathrm{r}} - g_1 < 0, \quad \text{(no contact)}, \end{cases} \tag{22}$$

$$H_{\mathrm{k}_2} = \begin{cases} 1, & x_{\mathrm{r}} + g_2 \leq 0, \quad \text{(contact with } k_2\text{)}, \\ 0, & x_{\mathrm{r}} + g_2 > 0, \quad \text{(no contact)}, \end{cases} \tag{23}$$

$$H_{\mathrm{fold}} = \begin{cases} 1, & x_{\mathrm{c}} - g_{\mathrm{b}} \geq 0, \quad \text{(contact with fold)}, \\ 0, & x_{\mathrm{c}} - g_{\mathrm{b}} < 0, \quad \text{(no contact)}. \end{cases} \tag{24}$$

Table 3
Operation modes of the capsule system and the corresponding values of the discrete variables H_{k_1}, H_{k_2}, H_{vel} and H_{fold} defined in (22)–(25).

Operation mode	H_{k_1}	H_{k_2}	H_{vel}	H_{fold}	Operation mode	H_{k_1}	H_{k_2}	H_{vel}	H_{fold}
{NCk, Vc0, NCb}	0	0	0	0	{Ck1, Vcp, Cb}	1	0	1	1
{NCk, Vc0, Cb}	0	0	0	1	{Ck1, Vcn, NCb}	1	0	−1	0
{NCk, Vcp, NCb}	0	0	1	0	{Ck1, Vcn, Cb}	1	0	−1	1
{NCk, Vcp, Cb}	0	0	1	1	{Ck2, Vc0, NCb}	0	1	0	0
{NCk, Vcn, NCb}	0	0	−1	0	{Ck2, Vc0, Cb}	0	1	0	1
{NCk, Vcn, Cb}	0	0	−1	1	{Ck2, Vcp, NCb}	0	1	1	0
{Ck1, Vc0, NCb}	1	0	0	0	{Ck2, Vcp, Cb}	0	1	1	1
{Ck1, Vc0, Cb}	1	0	0	1	{Ck2, Vcn, NCb}	0	1	−1	0
{Ck1, Vcp, NCb}	1	0	1	0	{Ck2, Vcn, Cb}	0	1	−1	1

$$H_{vel} = \begin{cases} 0, & v_c = 0 \ \text{ and } \ \left|f_0 + H_{k_1} f_1 + H_{k_2} f_2 + H_{fold} F_b(x_c)\right| \le 1, \ \text{ (capsule stationary)}, \\ 1, & v_c > 0 \ \text{ or } \ \left(v_c = 0 \ \text{ and } \ f_0 + H_{k_1} f_1 + H_{k_2} f_2 + H_{fold} F_b(x_c) > 1\right), \ \text{ (forward motion)}, \\ -1, & v_c < 0 \ \text{ or } \ \left(v_c = 0 \ \text{ and } \ f_0 + H_{k_1} f_1 + H_{k_2} f_2 + H_{fold} F_b(x_c) < -1\right), \ \text{ (backward motion)}, \end{cases} \tag{25}$$

where $x_c = x_m - x_r$ and $v_c = v_m - v_r$. Note that in the expressions above, the term $f_{mc} = f_0 + H_{k_1} f_1 + H_{k_2} f_2 + H_{fold} F_b(x_c)$ represents the force acting on the capsule from the internal mass and the fold. Therefore, if the capsule is stationary, whenever the force f_{mc} becomes greater than 1 or smaller than −1, the capsule will move forward or backward, respectively. For the numerical implementation, the discrete variables defined in (22)–(25) will be used to identify the specific operation mode of the capsule. Every operation mode will be associated to a triple $\{\Sigma, \Delta, \Theta\}$, where $\Sigma \in \{\text{NCk}, \text{Ck1}, \text{Ck2}\}$ (no contact with springs, contact with k_1, contact with k_2), $\Delta \in \{\text{Vc0}, \text{Vcp}, \text{Vcn}\}$ (capsule stationary, forward motion, backward motion) and $\Theta \in \{\text{NCb}, \text{Cb}\}$ (no contact with fold, contact with fold). For instance, the operation mode $\{\text{Ck2}, \text{Vcp}, \text{Cb}\}$ means that the capsule is moving forward with the internal mass in contact with the spring k_2 and the capsule in contact with a fold. In this way, the capsule system can operate under 18 different modes, as listed in Table 3.

4.2. Numerical study

In this section we will carry out a numerical investigation of the capsule response based on the mathematical formulation introduced in Section 4.1 (see system (21)), using the numerical continuation platform COCO [22]. Although model (21) is formulated using nondimensional parameters and variables, the numerical results will be presented in dimensions so as to better understand the practical implications. For a periodic response of the nondimensional capsule model (21) (with period $T > 0$) we introduce the quantity

$$\widetilde{V}_{avg} := \frac{1}{T}(x_c(T) - x_c(0)),$$

which gives the (nondimensional) average velocity per period of the capsule. According to formulae (20), the dimensional average velocity will be then given by $V_{avg} = \mu G \Omega_0 \widetilde{V}_{avg}/k$. Its sign indicates whether the capsule moves forwards (to the right) ($V_{avg} > 0$) or backwards (to the left) ($V_{avg} < 0$), see Fig. 1(e).

One of the main questions that will be addressed in this section is concerned with the conditions under which the capsule is able to cross a fold during operation. Specifically, we will try to identify a suitable combination of frequency and amplitude of external excitation in order to achieve a successful fold crossing. As a starting point for this study we will consider the initial solution displayed in Fig. 9(a), which corresponds to a stable periodic orbit with positive average capsule velocity V_{avg}, computed for the time window $t \in [0, 0.52]$ [s]. Via direct numerical integration this solution is extended to the larger interval $t \in [0, 1.3]$ [s], and in this way the capsule hits a fold located at $x_c = g_b$ at $t \approx 0.6892$ [s]. An important observation here is that, although the capsule hits the fold with positive V_{avg}, the device is not able to cross the fold and the system settles to another periodic solution impacting the initial part of the fold ($x_c = g_b$) repeatedly, see Fig. 9(b). Panel (c) shows the time history of the capsule force $F_{cap} = f_0 + H_{k_1} f_1 + H_{k_2} f_2$ (see (21)) representing the force acting on the capsule from the internal mass. In this way, positive and negative peaks can be observed, which correspond to impacts of the internal mass with the front (k_1) and back (k_2) springs, respectively, see Fig. 1(e).

In order to identify mechanisms under which a fold can be crossed, we will carry out a one-parameter continuation of the initial periodic solution shown in Fig. 9(a) with respect to the amplitude of excitation A. The result can be seen in Fig. 10(a). Here, the vertical axis displays the behaviour of the average capsule velocity V_{avg} as the amplitude A varies. During the continuation process, two critical points are detected. The first one, labelled F ($A \approx 209.96$ [mN]), stands for a fold bifurcation of limit cycles, where the periodic solution loses stability. Here, a branch of unstable periodic orbits is born (dashed line), unfolding towards the decreasing direction of the parameter. The second critical point, labelled P0 ($A \approx 209.02$ [mN]), corresponds to the excitation amplitude yielding $V_{avg} = 0$ [mm/s]. The points P1 and P2 shown on Fig. 10(a) are test points chosen so as to obtain positive and negative V_{avg}, respectively. These points, as can be observed

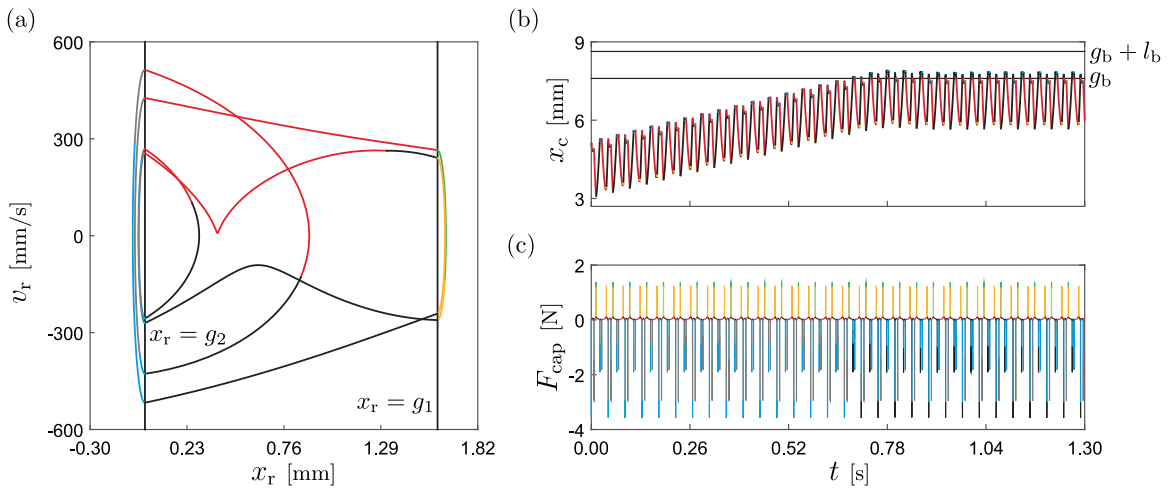

Fig. 9. (a) Periodic solution of the capsule model (21) (in dimensional form) computed for the time window $t \in [0, 0.52]$ [s] and the parameter values given in Table 1, with $\Omega/(2\pi) = 45$ [Hz], $A = 0.2098$ [N], $g_b = 8.31 \times 10^{-3}$ [m], $g_\ell = 26.71 \times 10^{-3}$ [m], $l_b = 1.033 \times 10^{-3}$ [m], $m_b = 5.31 \times 10^{-3}$ [m], $\beta_0 = -9.111 \times 10^{-2}$ [N/m], $\beta_1 = 3.918 \times 10^{4}$ [N/m^2], $\beta_2 = -1.925 \times 10^{7}$ [N/m^3], $\eta_0 = 6.945 \times 10^{-1}$ [N/m], $\eta_1 = 2.183 \times 10^{3}$ [N/m^2] and $\eta_2 = 2.106 \times 10^{5}$ [N/m^3]. The vertical black lines stand for the impact boundaries as shown in the figure. The different colours in panel (a) mark the solution segments as follows (see Table 3): $\{$Ck2, Vcp, NCb$\}$ (cyan), $\{$Ck2, Vcn, NCb$\}$ (grey), $\{$NCk, Vcn, NCb$\}$ (red), $\{$NCk, Vcp, NCb$\}$ (black), $\{$Ck1, Vcn, NCb$\}$ (green) and $\{$Ck1, Vcp, NCb$\}$ (yellow). Panel (b) presents the corresponding time plot extended for $t \in [0, 1.3]$ [s], showing the capsule position, using the colour code as in panel (a). Panel (c) displays the time history of the capsule force $F_{cap} = f_0 + H_{k_1} f_1 + H_{k_2} f_2$ (see (21)).

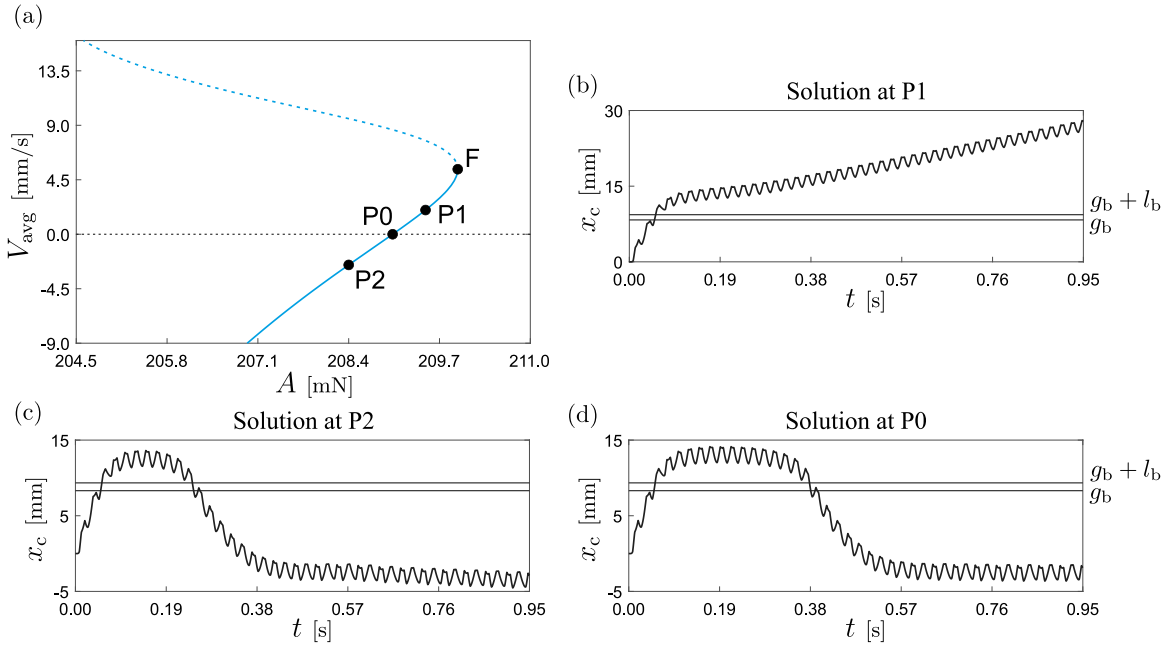

Fig. 10. (a) Numerical continuation of the periodic solution shown in Fig. 9(a) with respect to the excitation amplitude A. The vertical axis depicts the behaviour of the average capsule velocity V_{avg}. Dashed and solid lines represent unstable and stable solutions, respectively. The point F stands for a fold bifurcation of limit cycles located at $A \approx 209.96$ [mN], while P0 is a critical point where the average capsule velocity becomes zero (for $A \approx 209.02$ [mN]). The points P1 ($A = 209.5$ [mN]) and P2 ($A = 208.4$ [mN]) represent test points along the computed curve. Panels (b), (c) and (d) show time plots computed at the points P1, P2 and P0, respectively, with initial conditions $(x_m, v_m, x_r, v_r) = (0, 0, 0, 0)$.

in panels (b)–(d), can be used to identify a mechanism upon which a fold can be crossed, in the following sense. Starting from a reference resting position $(x_m, v_m, x_r, v_r) = (0, 0, 0, 0)$, the capsule can be steered to a final state where the average velocity is positive, zero or negative. If the amplitude A is chosen so that $V_{avg} < 0$ [mm/s], the capsule may initially move towards the fold due to the chosen initial conditions and external excitation, however, after some time the capsule behaviour is dominated by a stable periodic response with negative average velocity, in such a way that the capsule

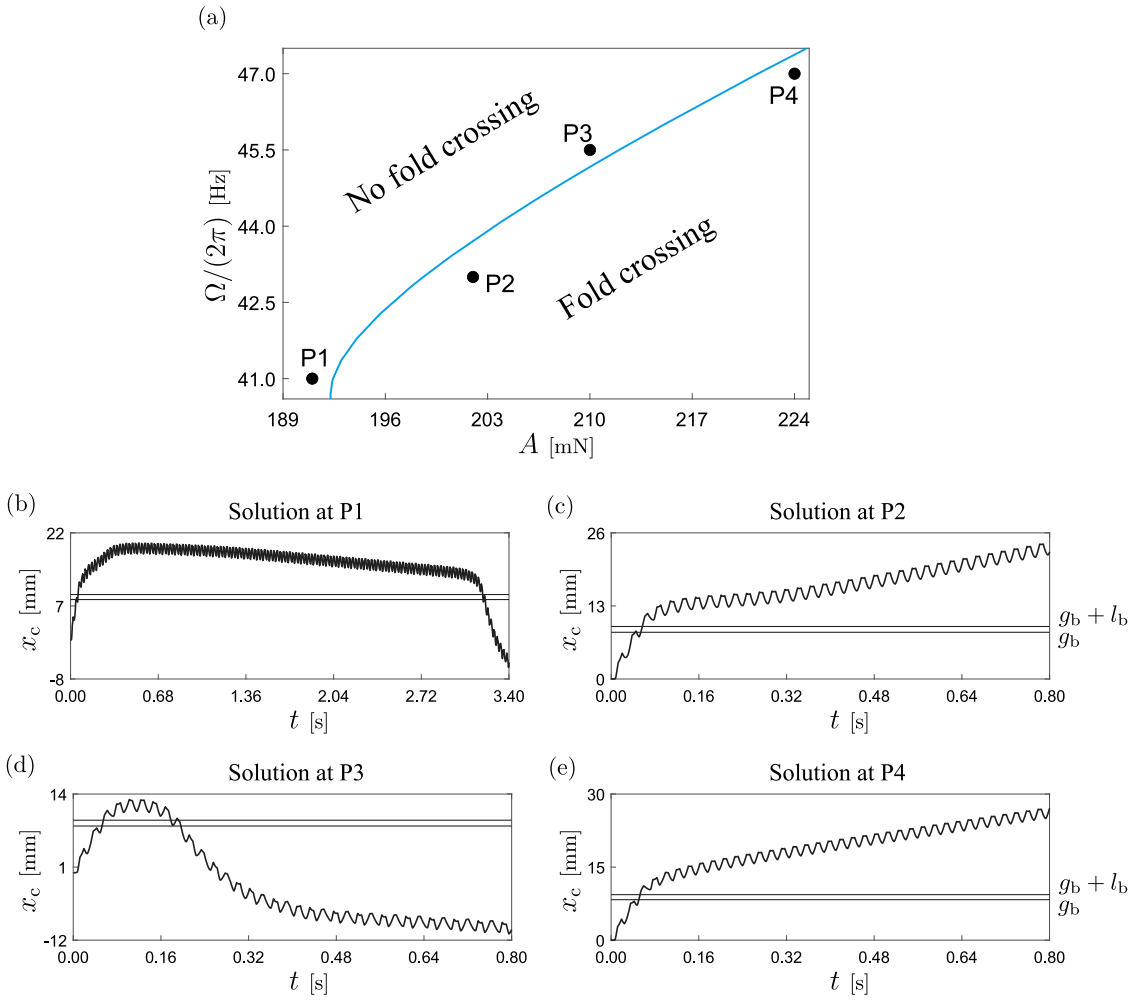

Fig. 11. Two-parameter continuation of the critical point P0 detected in Fig. 10(a) with respect to the amplitude and frequency of excitation. Panels (b)–(e) present capsule responses computed at the test points P1 ($A = 191$ [mN], $\Omega/(2\pi) = 41$ [Hz]), P2 ($A = 202$ [mN], $\Omega/(2\pi) = 43$ [Hz]), P3 ($A = 210$ [mN], $\Omega/(2\pi) = 45.5$ [Hz]) and P4 ($A = 224$ [mN], $\Omega/(2\pi) = 47$ [Hz]), with initial conditions $(x_m, v_m, x_r, v_r) = (0, 0, 0, 0)$.

eventually moves backwards and leaves the fold, as shown in the time history displayed in Fig. 10(c), computed at the test point P2. Panel (d) depicts the capsule motion at the critical point P0, showing that the capsule settles to a periodic solution with $V_{avg} = 0$ [mm/s], which can be considered as a limiting case. On the other hand, Fig. 10(b) presents the capsule behaviour at P1 where $V_{avg} > 0$ [mm/s], thereby illustrating a case for which the fold is fully crossed due to the positive average capsule velocity that is achieved after the transients have decayed.

Based on the fold crossing strategy proposed above, we will now try to identify a suitable combination of control parameters (frequency and amplitude of excitation) that can be employed for this purpose. To this end, we will carry out a two-parameter continuation of the P0-periodic solution computed before with respect to frequency and amplitude, imposing the condition $V_{avg} = 0$ [mm/s]. The result of this process is presented in Fig. 11(a). Here, the computed curve represents a family of periodic solutions with zero average velocity, as the one observed in Fig. 10(d). In this way, the resulting curve divides locally the parameter space into two regimes: the upper one where the capsule is not able to cross the fold and the lower region where a successful crossing can be achieved. The effectiveness of the proposed crossing strategy is illustrated in panels (b)–(e), where a series of test points are chosen both on the upper and lower regions described before.

The boundary of fold crossing obtained by the continuation strategy is then compared with the simulation for validation. As displayed in Fig. 12(a), the simulation by using either Eq. (14) or (15) yields the same result. In addition, the boundary has a comparatively consistent prediction of the fold crossing, although it is not exactly the same as the simulation result. This is possibly due to the reason that the fold crossing is significantly influenced by the transient phase of the capsule dynamics, which cannot be perfectly defined in the continuation method.

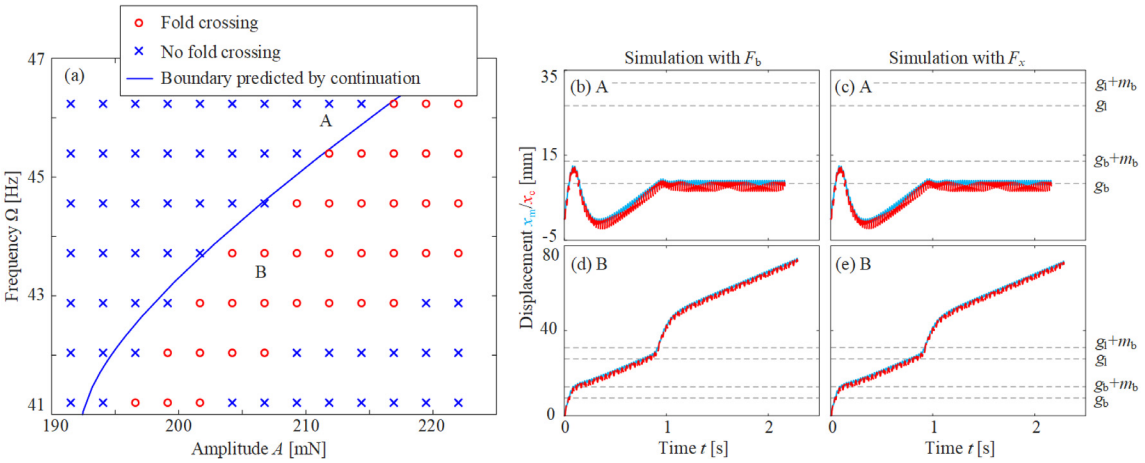

Fig. 12. (a) Boundary dividing the results of fold and no fold crossings. Time series for two groups of parameters marked as Points A and B are shown in Panels (b-e), showing that simulation with either F_x or F_b, Eq. (14) or (15), yields the same result.

5. Conclusions

This paper has studied a capsule periodically driven by a vibro-impact oscillator moving on a small intestine substrate with various circular folds. The resistance force exerted on the capsule was first obtained by integrating the pressure on the capsule shell, and was then simplified by approximating it with piecewise polynomials.

The steady state of capsule responses was studied by using bifurcation analysis, showing that the geometry and mechanical properties of the folds do not have a significant influence on the bifurcation patterns. However, they significantly changes the progression of the capsule. In general, a larger and stiffer fold is much harder to be crossed by the capsule. In general, the fold has no influence on the capsule dynamics if its steady state corresponds with a backward motion. However, a small and soft fold could change the capsule response if it is crossed in the transient phase, but stops the capsule's return journey thereafter.

The frequency and amplitude of the excitation have a crucial influence on the capsule response. The bifurcation pattern is very simple for $\Omega = 55$ [Hz], where the majority of the capsule response corresponds with a P-1-1-0 backward progression. Only a small region for coexisting forward progression by P-1-2-1 and P-2-4-2 motions was observed for $A > 150$ [mN]. The bifurcation becomes extremely complex for $\Omega = 45$ [Hz], which reveals points of periodic doubling, regions of multiple stability, and irregular dynamics. In general, the capsule performs a backward (forward) motion for small (large) excitation amplitude. For $\Omega = 35$ [Hz], the capsule has a relatively simple backward motion for small excitation, which becomes complex when the excitation is strong. More specifically for $A > 211$ [mN], the capsule crossed the folds during the transient phase, but its steady state of backward motion was stopped by the folds thereafter.

Finally, numerical study of the bifurcation via continuation method was performed with COCO and nondimensional governing equation of the capsule dynamics. The resistance force from the capsule-fold contact was replaced by a piecewise nonlinear spring, and the capsule dynamics was distributed into 18 operation modes according to the non-smoothness. In addition, the mechanism of fold crossing was defined as the critical point for zero progression velocity. Compared with direct numerical simulation, this method yielded a consistent prediction of the fold crossing. However, this prediction is not perfect, which could be due to the significance of transient phase for the fold crossing.

CRediT authorship contribution statement

Yao Yan: Conceptualization, Methodology, Software, Validation, Formal analysis, Investigation, Writing – original draft, Visualization, Funding acquisition. **Baoquan Zhang:** Software, Validation, Formal analysis, Investigation, Writing – original draft, Visualization. **Joseph Páez Chávez:** Methodology, Software, Validation, Formal analysis, Investigation, Writing – original draft, Visualization. **Yang Liu:** Conceptualization, Methodology, Writing – review & editing, Visualization, Supervision, Project administration, Funding acquisition.

Declaration of competing interest

The authors declare that they have no known competing financial interests or personal relationships that could have appeared to influence the work reported in this paper.

Data accessibility

The numerical data sets generated and analysed during the present study are available from the corresponding author on reasonable request.

Acknowledgements

This work has been supported by EPSRC under Grant No. EP/V047868/1. Professor Yao Yan would like to acknowledge the financial support from National Natural Science Foundation of China (Grants No. 11872147 and 12072068).

References

[1] Iddan G, Meron G, Glukhovsky A, Swain P. Wireless capsule endoscopy. Nature 2000;405(6785):417.
[2] Slawinski PR, Obstein KL, Valdastri P. Capsule endoscopy of the future: What's on the horizon? World J Gastroenterol 2015;21(37):10528.
[3] Singeap AM, Stanciu C, Trifan A. Capsule endoscopy: The road ahead. World J Gastroenterol 2016;22(1):369.
[4] Hao Y, Li J, Bianchi F, Zhang P, Ciuti G, Dario P, et al. Analytical magnetic model towards compact design of magnetically-driven capsule robots. IEEE Trans Med Robot Bionics 2020;2:188–95.
[5] Shi Q, Liu T, Song S, Wang J, Meng M. An optically aided magnetic tracking approach for magnetically actuated capsule robot. IEEE Trans Instrum Meas 2021;70:4003009.
[6] Erin O, Alici C, Sitti M. Design, actuation, and control of an MRI-powered untethered robot for wireless capsule endoscopy. IEEE Robot Autom Lett 2021;6(3):6000–7.
[7] Zhou H, Alici C. A novel magnetic anchoring system for wireless capsule endoscopes operating within the gastrointestinal tract. IEEE/ASME Trans Mechatronics 2019;24(3):1106–16.
[8] Liu Y, Wiercigroch M, Pavlovskaia E, Yu H. Modelling of a vibro-impact capsule system. Int J Mech Sci 2013;66:2–11.
[9] Liu Y, Pavlovskaia E, Hendry D, Wiercigroch M. Vibro-impact responses of capsule system with various friction models. Int J Mech Sci 2013;72:39–54.
[10] Guo B, Liu Y, Birler R, Prasad S. Self-propelled capsule endoscopy for small-bowel examination: Proof-of-concept and model verification. Int J Mech Sci 2020;174:105506.
[11] Liu Y, Páez Chávez J, Zhang J, Tian J, Guo B, Prasad S. The vibro-impact capsule system in millimetre scale: Numerical optimisation and experimental verification. Meccanica 2020;55(10):1885–902.
[12] Liu Y, Tian J, Manfredi L, Terry B, Prasad S, Rahman I, Marlicz W, Koulaouzidis A. A survey of small bowel modelling and its applications for capsule endoscopy. Mechatronics 2022;83:102748.
[13] Smith ME, Morton DG. The digestive system: Systems of the body series. second ed.. China: Churchill Livingstone; 2010.
[14] Barducci L, Norton JC, Sarker S, Mohammed S, Jones R, Valdastri P, et al. Fundamentals of the gut for capsule engineers. Progr Biomed Eng 2020;2(4):042002.
[15] Yan Y, Liu Y, Manfredi L, Prasad S. Modelling of a vibro-impact self-propelled capsule in the small intestine. Nonlinear Dynam 2019;96(1):123–44.
[16] Tian J, Liu Y, Chen J, Guo B, Prasad S. Finite element analysis of a self-propelled capsule robot moving in the small intestine. Int J Mech Sci 2021;206:106621.
[17] Guo B, Liu Y, Prasad S. Modelling of capsule–intestine contact for a self-propelled capsule robot via experimental and numerical investigation. Nonlinear Dynam 2019;98(4):3155–67.
[18] Guo B, Ley E, Tian J, Zhang J, Liu Y, Prasad S. Experimental and numerical studies of intestinal frictions for propulsive force optimisation of a vibro-impact capsule system. Nonlinear Dynam 2020;101(1):65–83.
[19] Sliker LJ, Ciuti G, Rentschler ME, Menciassi A. Frictional resistance model for tissue-capsule endoscope sliding contact in the gastrointestinal tract. Tribol Int 2016;102:472–84.
[20] Guo B, Liu Y. Three-dimensional map for a piecewise-linear capsule system with bidirectional drifts. Physica D 2019;399:95–107.
[21] Guo B, Páez Chávez J, Liu Y, Liu C. Discontinuity-induced bifurcations in a piecewise-smooth capsule system with bidirectional drifts. Commun Nonlinear Sci Numer Simul 2021;102:105909.
[22] Dankowicz H, Schilder F. Recipes for continuation. Computational science and engineering, Philadelphia: SIAM; 2013.
[23] Doedel EJ, Champneys AR, Fairgrieve TF, Kuznetsov YA, Sandstede B, Wang X-J. Auto97: Continuation and bifurcation software for ordinary differential equations (with HomCont). 1997, Computer Science, Concordia University, Montreal, Canada, Available at http://cmvl.cs.concordia.ca.
[24] Dhooge A, Govaerts W, Kuznetsov YA. MATCONT: A MATLAB package for numerical bifurcation analysis of ODEs. ACM Trans Math Software 2003;29(2):141–64.
[25] Páez Chávez J, Liu Y, Pavlovskaia E, Wiercigroch M. Path-following analysis of the dynamical response of a piecewise-linear capsule system. Commun Nonlinear Sci Numer Simul 2016;37:102–14.
[26] Xu J, Fang H. Improving performance: Recent progress on vibration-driven locomotion systems. Nonlinear Dynam 2019;98:2651–69.
[27] Fang H, Xu J. Stick-slip effect in a vibration-driven system with dry friction: Sliding bifurcations and optimization. J Appl Mech 2014;81:051001.
[28] Nunuparov A, Becker F, Bolotnik N, Zeidis I, Zimmermann K. Dynamics and motion control of a capsule robot with an opposing spring. Arch Appl Mech 2019;89:2193–208.
[29] Zimmermann K, Zeidis I, Lysenko V. Mathematical model of a linear motor controlled by a periodic magnetic field considering dry and viscous friction. Appl Math Model 2021;89:1155–62.
[30] Nguyen K, La N, Ho K, Ngo Q, Chu N, Nguyen V. The effect of friction on the vibro-impact locomotion system: Modeling and dynamic response. Meccanica 2021;56:2121–37.
[31] Chernousko F. Two-dimensional motions of a body containing internal moving masses. Meccanica 2016;51:3203–9.
[32] Zhan X, Xu J, Fang H. Planar locomotion of a vibration-driven system with two internal masses. Appl Math Model 2016;40:871–85.
[33] Zhang J, Tian J, Zhu D, Liu Y, Prasad S. Design and experimental investigation of a vibro-impact self-propelled capsule robot with orientation control. In: 2022 IEEE international conference on robotics and automation. 2022, p. 1–7.
[34] Zarychta S, Sagan T, Balcerzak M, Dabrowski A, Stefanski A, Kapitaniak T. A novel, Fourier series based method of control optimization and its application to a discontinuous capsule drive model. Int J Mech Sci 2022;219:107104.
[35] Liu P, Yu H, Cang S. Optimized adaptive tracking control for an underactuated vibro-driven capsule system. Nonlinear Dynam 2018;94:1803–17.
[36] Liao M, Zhang J, Liu Y, Zhu D. Speed optimisation and reliability analysis of a self-propelled capsule robot moving in an uncertain frictional environment. Int J Mech Sci 2022;221:107156.